Nanoscale Advances

Accepted Manuscript

This article can be cited before page numbers have been issued, to do this please use: K. Tao, M. Han, L. Jiang, S. Jin, T. Giovannini, D. Garoli, Z. Zhao, Q. Lin and H. jin, *Nanoscale Adv.*, 2026, DOI: 10.1039/D6NA00164E.

ROYAL SOCIETY OF CHEMISTRY

rsc.li/nanoscale-advances

View Article Online
DOI: 10.1039/D6NA00164E

In-situ SERS Reveals Nickel Hydroxide Formation in PtRuNi Catalysts Enhancing Hydrogen Oxidation

Kai Tao[a], Mingxiao Han[b], Li Jiang[b] ,Shangzhong Jin[b], Tommaso Giovannini[c], Denis Garoli[b,d*], Zhefei Zhao[e], Qiang Lin[f], Huaizhou Jin[a*]

[a] Key Laboratory of Quantum Precision Measurement, College of Physics, Zhejiang University of Technology, Hangzhou 310014, China.

[b] College of Optical and Electronic Technology, China Jiliang University, Hangzhou 310018, China.

[c] Department of Physics, University of Rome Tor Vergata, and INFN, Via della Ricerca Scientifica 1, I-00133, Rome, Italy

[d] Dipartimento di Scienze e Metodi dell'Ingegneria, Università degli Studi di Modena e Reggio Emilia, Viale Amendola 2, Reggio Emilia (Italy)

[e] Department of Applied Chemistry, Petroleum and Chemical Industry Key Laboratory of Organic Electrochemical Synthesis, State Key Laboratory of Green Chemical Synthesis and Conversion, Zhejiang University of Technology, Hangzhou 310014, China.

[f] State Key Laboratory of Ocean Sensing & Institute of Quantum Sensing & School of Physics, Zhejiang University, Hangzhou, 310058, China

Corresponding authors: Huaizhou Jin - jinhuaizhou@zjut.edu.cn; Prof. Denis Garoli – denis.garoli@unimore.it

Abstract

Understanding the mechanisms for improving hydrogen oxidation reaction (HOR) activity on Pt-based catalysts in alkaline environment is challenging due to the lack of directly observed intermediates. Understanding the role of oxophilic metal additives is also crucial for designing advanced catalysts. In this study, we use *in situ* surface-enhanced Raman spectroscopy (SERS) to investigate HOR on Au@PtRuNi nanoparticles. Electrochemical measurements show improved HOR activity with little change in hydrogen binding energy (HBE), whereas Raman results show the 740 cm^{-1} peak for hydroxyl adsorption on Ru, as well as a new peak at 565 cm^{-1}, which can likely be attributed to the formation of nickel hydroxide ($Ni(OH)_2$) during the catalytic process, starting from 0.3 to 0.5V vs RHE. This suggests that nickel hydroxide and the hydroxyl groups on ruthenium likely collaborate to facilitate hydrogen oxidation.

1. Introduction

Hydrogen fuel cells are a promising technology for green energy generation; they are highly efficient and produce only water as a byproduct, making them environmentally friendly [1–4]. One critical half-reaction in hydrogen fuel cells is the hydrogen oxidation reaction (HOR). In fact, the efficiency of this reaction is significantly influenced by the electrocatalyst [5–8]. Platinum (Pt) is a well-known electrocatalyst in HOR; however, because of its scarcity and high cost, researchers are actively exploring other metals and alloys to enhance catalytic activity and reduce costs [9–11]. In recent years, alkaline anion exchange membrane fuel cells (AEMFCs) have gained significant

View Article Online
DOI: 10.1039/D6NA00164E

attention due to their ability to work better with non-platinum group metal catalysts [12–15]. However, HOR is significantly slower in alkaline media than in acid. Therefore, researchers are trying to develop new catalysts that can operate efficiently in alkaline environments [16]. Among them, ruthenium (Ru) and nickel (Ni) are two particularly promising candidates for enhancing Pt-based catalyst performance [17–19]. Studies have also shown that multi-metal catalysts, such as those formed by implanting oxophilic metals into PtRu structures, can enhance HOR activity; however, their mechanisms have not yet been fully elucidated [20].

To understand HOR in alkaline media, we first start with its reaction equation. HOR in alkaline media consists of a few basic steps: Tafel, Heyrovsky, and Volmer steps, with the first step being the Tafel or Heyrovsky process, and the second being the Volmer process [17,21]. The reaction equations of Tafel, Heyrovsky and Volmer steps are shown in (1) to (3), with the total reaction equation shown in equation (4):

Tafel step	$* + H_2 \rightarrow 2H_{ad}$	(1)
Heyrovsky step	$* + H_2 + OH^- \rightarrow H_{ad} + H_2O + e^-$	(2)
Volmer step	$H_{ad}+OH^- \rightarrow * + H_2O + e^-$	(3)
Total equation	$2* + H_2 + 2OH^- \rightarrow 2* + 2H_2O + 2e^-$	(4)

In these equations, * represents hydrogen adsorption sites. Heyrovsky and Volmer steps involve the participation of hydroxyl (OH) species. The source of OH^- species as well as its precise role remain areas of active investigation and debate [22,23]. The two dominant mechanistic proposals are the hydrogen binding energy (HBE) theory and the bifunctional mechanism [24]. Supporters of HBE theory emphasize that the hydrogen binding energy is the primary factor that affects HOR kinetics [25]. On the other hand, supporters of the bifunctional mechanism postulate that HOR kinetics in alkaline media is limited by the Volmer step, and that adsorbed OH species on oxophilic metal or compound sites on the electrocatalysts would enhance HOR activity by facilitating the Volmer step [26]. One of the earliest supporters of the bifunctional mechanism, Nenad M. Markovic's group, successfully modified Pt(111) with $Ni(OH)_2$-islands, and suggested that adsorbed OH species is a key reactant in the HOR in alkaline solutions [27]. One critical reason for this debate stems from the technical challenges in directly observing the short-lived hydroxyl intermediates during the catalysis [28–30]. Surface-enhanced Raman spectroscopy (SERS) is a powerful tool for identifying and characterizing these transient species at the electrode-electrolyte interface (i.e. *in situ*) [31]. This technique can be employed to identify adsorbed hydroxyl species and other intermediates, providing direct spectroscopic evidence to elucidate their role in the reactions [5]. In several previous studies, Ru has been identified as a key oxophilic metal for OH adsorption, with the metal's ability to adsorb OH species at very low potentials [32,33]. Specifically, SERS results indicated that the formed ruthenium oxides served as robust OH adsorption sites, thereby facilitating the HOR process [33]. Ni can also provide OH adsorption sites, but the adsorption may happen at a higher potential [34].

In this study, we aim to utilize SERS to investigate the behavior of adsorbed hydroxyl intermediates on Pt and PtRu based catalysts by using Au@Pt, Au@PtRu and Au@PtRuNi core-shell structures [35]. Au@PtRuNi structure is used to investigate the role of Ni in the HOR process, and that whether Ni can act in synergy with Ru to improve HOR activity. The Au@PtRuNi core-shell structure is shown in Figure 1. This comparative analysis with multiple catalysts using both electrocatalytic measurement and SERS allows for a nuanced understanding of how different oxophilic elements influence the interfacial interactions in HOR, and allowed us to discover possible nickel hydroxide formation which facilitates the HOR process.

2. Materials and Methods

2.1 Materials and Instrumentation

Gold chloride trihydrate ($HAuCl_4 \cdot 3H_2O$, 99.9%) is the precursor used to synthesize gold nanoparticles (AuNPs). Metal precursors used for catalysis synthesis include chloroplatinic acid hexahydrate ($H_2PtCl_6 \cdot 6H_2O$, 99.9%),

View Article Online
DOI: 10.1039/D6NA00164E

ruthenium (III) chloride hydrate ($RuCl_3 \cdot xH_2O$), and nickel chloride hexahydrate ($NiCl_2 \cdot 6H_2O$).

Reductive agents include sodium borohydride ($NaBH_4$), ascorbic acid and sodium citrate were employed for the synthesis; ethanol, potassium hydroxide, and ultrapure water (18.2 MΩ cm) were used for solution preparation and cleaning procedures.

All reagents above are purchased from various domestic providers, such as Adamas-beta, Macklin and Aladdin, all from Hangzhou and Shanghai, China. They are all analytical grade and were used without further purification. Vulcan carbon XC-72 was utilized as the catalyst support material, obtained from Cabot Corporation, Boston, United States.

Electrochemical measurements were performed using a DHElecchem electrochemical workstation with a standard three-electrode setup, using the built-in DHElecchem software to record electrochemical data. A Gauss Union C031-4 in-situ electrochemical flowcell was used for all electrochemical and in-situ Raman measurements. The flowcell was equipped with a standard tri-electrode setup, including a platinum wire counter electrode, a mercury/mercurous oxide (Hg/HgO) reference electrode, and a glassy carbon working electrode, with all potentials referenced against the reversible hydrogen electrode (RHE) in 0.1 M KOH solution.

For Raman measurements, we are using Horiba Xplora Raman Spectrometer (Horiba Jobin Yvon, Paris, France). 638 nm laser was used as the excitation laser. Strong fluorescent interference was present for SERS measurements when 532nm laser was used; on the other hand, the signals we obtain when using 785nm laser was too weak.

2.2 Methods

Synthesis of 55nm AuNPs. The 55nm AuNPs are synthesized according to Frens' method [36,37]. Specifically, 2.424 mL of 0.825% $HAuCl_4$ aqueous solution was combined with 196 mL of water in a Three-necked round-bottom flask. This mixture was subsequently brought to a boil, followed by the rapid addition of 1.5 mL of 1% trisodium citrate solution under continuous stirring while boiling for 20 minutes. The resulting colloidal solution was then cooled to room temperature and stored for further use.

Synthesis of Au@Pt nanoparticles. Core-shell Au@Pt nanoparticles were synthesized following similar steps as reported in previous chemical reduction methods [33,34]. Specifically, Au@Pt nanoparticles were synthesized by first combining 30 mL of gold colloidal solution with 0.72 mL of 1 mM aqueous H_2PtCl_6; this mixture was then stirred at 80°C, followed by the dropwise addition of 0.36 mL of 10 mM aqueous ascorbic acid using a step motor-controlled syringe. Stirring was maintained for an additional 20 minutes after the complete addition.

Synthesis of Au@PtRu nanoparticles. After synthesis of Au@Pt nanoparticles, Ru was reduced on to the surface by adding 120µL of 1mM $RuCl_3$ and 60µL of 1% trisodium citrate quickly while the solution was boiling. The solution is then stirred while boiling for another 20 minutes to complete the reduction process, forming Au@PtRu.

Synthesis of Au@PtRuNi nanoparticles. For Au@PtRuNi nanoparticles, Pt and Ni were reduced on the surface of AuNPs simultaneously by combining 30 mL of gold colloidal solution with 0.72 mL of 1 mM aqueous H_2PtCl_6 and 0.72mL of 1mM aqueous $NiCl_2$ solution. This mixture was then stirred at 80°C, followed by the dropwise addition of 0.72 mL of 10 mM aqueous ascorbic acid using a step motor-controlled syringe, and stirring was maintained for an additional 20 minutes after the complete addition. Then, Ru was reduced on to the surface using exactly the same method in the synthesis of Au@PtRu nanoparticles.

After synthesis of these Au@catalyst core-shell nanoparticles, transmission electron microscopy (TEM) was used to characterize their morphology and size distribution of the nanoparticles, with elemental composition and mapping characterized by Energy-dispersive X-ray spectroscopy (EDS). Additionally, electrochemical techniques such as cyclic voltammetry (CV) and linear sweep voltammetry were employed to evaluate the catalytic activity with the aforementioned DHElecchem electrochemical workstation. In-situ Raman Spectroscopy measurements

View Article Online
DOI: 10.1039/D6NA00164E

were conducted under constant potential conditions (such as -0.015V, 0.035V, 0.085V, 0.135V …) to investigate intermediates during the electrochemical processes.

3. Results

3.1 Characterization of Nanoparticles

Figure 2 shows the characterization results of Au@PtRuNi nanoparticles. Figure 2(a) and (b) show the TEM result of the nanoparticles. The TEM images suggest that chemical reduction method produced uniform nanoparticles with an average diameter of 30nm and well-defined morphology.

EDS elemental mapping reveals the spatial distribution of Au, Pt, Ru, and Ni throughout the nanoparticles. Figure 2(c) shows the distribution of the four individual metals. The Au and Pt signals are concentrated in the center of the figure, this suggests more continuous distribution of Au and Pt, whereas the Ru and Ni signals are spread more sparsely over the nanoparticle. Quantitative EDS analysis of Au, Pt, and Ru shows atomic percentages of 77.80%, 21.01%, and 1.18%, respectively (normalized for Au, Pt and Ru only). Nickel content could not be accurately quantified by EDS; however, the presence of nickel content is confirmed in XPS results in Figure 3(c) and (d). In fact, X-ray photoelectron spectroscopy (XPS) was used to characterize the surface chemical states of the Au@PtRuNi nanoparticles, as shown in Figure 3. The Pt4f spectrum displays two prominent peaks at binding energies of 71.2 eV (Pt $4f_{7/2}$) and 74.5 eV (Pt $4f_{5/2}$), which correspond to metallic Pt, with a minor shoulder at ~72.3 eV suggesting the presence of partially oxidized Pt species Pt(II). The Ru $3p_{3/2}$ peak is observed at 462.9 eV, consistent with metallic Ru, while a broadening toward higher binding energy indicates a small fraction of RuO_x, which is in agreement with the role of Ru as an oxophilic site for OH adsorption. XPS spectra of Ni 2p are taken both before and after HOR. In Figure 3(c), two main Ni $2p_{3/2}$ peaks appear at 856.0 eV and 852.7 eV corresponding to Ni(II) and metallic Ni, respectively. XPS results further show that the deposition of Pt, Ru and Ni on the Au core is successful. In addition, as shown in Figure 3(d), the XPS curve changes after HOR electrocatalysis. The 852.7 eV peak corresponding to metallic Ni disappears while the 855.6 eV peak, which corresponds to Ni(II), becomes the main Nickel peak in the spectrum. The shift of the satellite peak from 860.3 to 862.3 eV also suggests that Nickel species are oxidized during the HOR process.

3.2 Electrocatalytic Performances

Figure 4(a) shows the HOR cyclic voltammetries (CV) result of HOR on Au@Pt, Au@PtRu and Au@PtRuNi nanoparticles. CV are measured in the range from 0.0 to 1.0 V vs. RHE at a scan rate of 10 mV/s in 0.1 M KOH solution saturated with H_2. On all CV curves, we can see hydrogen underpotential deposition (H_{upd}) peaks around 76 mV. This means the addition of oxophilic metals on the Pt layer did not alter the hydrogen binding energy (HBE) significantly. On the CV curve of Au@PtRuNi, there are exclusive metal redox peaks at 0.77 and 0.88 V. According to Hall et al and Oshchepkov et al, redox peaks in this region can be assigned to the transition between α-$Ni(OH)_2$ and β-$Ni(OH)_2$ [38–40].

The CV curves in Figure 4(a) also show that Au@PtRuNi exhibits a higher double-layer capacitance (Cdl) compared to Au@PtRu and Au@Pt; the increased Cdl may arise from enhanced surface roughness and/or hydrophilicity from $Ni(OH)_2$ formation.

In order to assess the catalytic performance of the three catalysts, we also performed polarization experiments. Figure 4(b) shows the polarization curves of Au@Pt, Au@PtRu and Au@PtRuNi catalysts obtained from linear sweeping voltammetry in 0.1 M KOH with saturated H_2 at a sweeping rate of 10 mV/s and rotating speed of 1600 rpm, with inset of Figure 4(b) showing the micro-polarization regions of -4 to 4 mV. Figure 4(c) shows the Tafel plot obtained from the LSV data from Figure 4(b). Current densities increase faster for Au@PtRuNi than for

View Article Online
DOI: 10.1039/D6NA00164E

Au@PtRu and Au@Pt, with Au@Pt having the slowest increasing of current density. At a fixed current density of 1 mA/cm², Au@PtRuNi requires an overpotential of 38.9 mV, compared to 52.5 mV for Au@PtRu and 65.5 mV for Au@Pt. This 13.6 mV and 26.6 mV improvement over Au@PtRu and Au@Pt, respectively, demonstrates that the catalytic enhancement arises from electronic and chemical effects of $Ni(OH)_2$, rather than the increase of surface area and hydrophilicity alone.

These results demonstrate that the inclusion of Ni in the catalyst provides genuine catalytic enhancement. The mechanisms of this enhancement is revealed by our in-situ SERS analysis in the next section.

3.3 SERS measurement results

We further examine the catalytic mechanics using in-situ electrochemical SERS. Figure 5(a) shows a comparison between the SERS spectra obtained from Au@Pt, Au@PtRu, Au@PtRuNi alloy nanoparticles at a potential set to 0.155 V. Compared to Au@Pt NPs, Au@PtRu and Au@PtRuNi nanoparticles have a clear additional peak at 740 cm^{-1}. This peak was reported in literature and was attributed to OH_{ad} species adsorbed on Ru or RuO_x [33]. Au@PtRu and Au@PtRuNi having the same 740 cm^{-1} peaks indicates that Ru or RuO_x are a primary OH adsorption site.

The changes to spectra of HOR on Au@PtRuNi nanoparticles from -0.015 V to 0.535 V (-15 to 535 mV) vs RHE are shown in Figure 5(b). In these experiments, we also found another peak at 566 cm^{-1} that becomes stronger as potential increases. In Au@PtRu results in Figure 5(c), a peak may also be found near 566 cm^{-1}. However, the 566 cm^{-1} peak obtained from the Au@PtRu catalyst becomes weaker as potential increases, and disappears before 0.2V, which is attributed to the oxidation of RuO_x and is consistent with previous results [33]. On the other hand, for experiments on Au@PtRuNi nanoparticles, the intensity of 566 cm^{-1} increases as the potential increases, especially at and above 0.385V vs RHE. Hence, the increasing 566 cm^{-1} peak on Au@PtRuNi nanoparticles is associated primarily with Ni compounds. Nickel has two primary (oxy)hydroxide species in electrochemistry: nickel hydroxide, $Ni(OH)_2$, where Ni is predominantly in the +2 oxidation state, or Ni(II), and nickel oxyhydroxide, NiOOH, which contains nickel in the +3 oxidation state, or Ni(III). Our post-reaction XPS result in Figure 3(d) shows a prominent Ni(II) peak at 855.6 eV; the metallic Ni peak, which is present in the pre-reaction XPS curve in Figure 3(c), disappears in Figure 3(d), suggesting that most Ni species are oxidized. We performed peak fitting on the post-reaction XPS result, and the fit could not converge when a Ni(III) peak was added. This suggests that the contribution of Ni(III) is non-existent or extremely minimal, and that Ni(II) is the dominant nickel species in the HOR process. In literature, the formation of NiOOH or Ni(III) typically require higher potentials; 1.2V to 1.4V vs RHE is the minimum potentials required for NiOOH formation, whereas $Ni(OH)_2$ can form at lower potentials, such as at 0.5V vs RHE [41,42]. According to recent studies, transition of α-$Ni(OH)_2$ to β-$Ni(OH)_2$ can takes place at low potentials, which is a phenomenon consistent with the two distinct oxidation peaks observed in the cyclic voltammetry curve of Au@PtRuNi; moreover, Hall et al. assigned the peak around 566 cm^{-1} to β-$Ni(OH)_2$, and α-$Ni(OH)_2$ exhibits no such pears near that region [38,43]. Xue et al also showed in a RuNi/C catalyst, Ni species are present as oxidized Ni(II) under operating conditions [44]. Given these evidences, we attribute the 566 cm^{-1} peak on Au@PtRuNi to be $Ni(OH)_2$. The distinct behavior of the 566 cm^{-1} peak in the Au@PtRuNi system, intensifying with increasing potential, suggests the potential involvement of nickel hydroxide species, that it may enhance the HOR catalytic activity.

We also performed peak-fitting for the 740 cm^{-1} peak on Au@PtRuNi and Au@PtRu catalysts; the results (Supplementary Figure S2) show that the area of the 740 cm^{-1} peak on Au@PtRuNi is larger at lower potentials and gradually decreases as the potential increases, whereas the 740 cm^{-1} band on Au@PtRu remains similar over the same potential range. This potential-dependent decrease in 740 cm^{-1} peak area on Au@PtRuNi, while remaining constant on Au@PtRu, indicates that the addition of nickel fundamentally modifies the OH_{ad} adsorption dynamics.

View Article Online
DOI: 10.1039/D6NA00164E

Here, we propose that $Ni(OH)_2$ acts as a dual-function modifier. First, it facilitates water activation and supplies additional OH_{ad} species through its inherent oxophilic character; secondly, it creates favorable interfacial sites at the $Ni(OH)_2$-RuO_x perimeter for efficient OH_{ad} consumption. At lower potentials (-0.015 to 0.235 V vs RHE), the enhanced OH_{ad} generation dominates, resulting in a larger 740 cm^{-1} peak on Au@PtRuNi compared to Au@PtRu. However, at higher potentials (above 0.235 V vs RHE), OH_{ad} is consumed more rapidly through the interfacial Volmer step at Pt-RuO_x sites promoted by $Ni(OH)_2$, causing the 740 cm^{-1} peak to decrease. The potential role of $Ni(OH)_2$ will be further discussed in the discussions section.

4. Discussions

The HOR in-situ SERS results on Au@PtRuNi catalyst provide clear evidence that Ru/RuO_x is still the dominant OH_{ad} adsorption site, whereas Ni in Au@PtRuNi is oxidized into hydroxide or oxyhydroxide phases, most likely $Ni(OH)_2$, as evidenced by the 566 cm^{-1} peak. The presence of the potential-dependent 566 cm^{-1} peak, as well as the potential-dependent decrease in the 740 cm^{-1} OH_{ad} peak area on Au@PtRuNi, suggest a bifunctional mechanism in which Ru/RuO_x and $Ni(OH)_2$ play distinct yet complementary roles. Lin et al showed OH_{ad} adsorbed on to the surface of RuO_x has favorable free energy to react with H_{ad} to form H_2O ($\Delta G \approx -0.7$ eV) [33]. This places RuO_x close to the optimal OH_{ad} binding region for alkaline HOR [45,46]. With the bifunctional mechanism, Pt provides sites for the adsorption of hydrogen atoms and form H_{ad}, while RuO_x supplies optimally bound OH_{ad} that reacts with H_{ad} to form H_2O. Our SERS observation that the position of 740 cm^{-1} peak being unchanged upon Ni addition indicates that the Pt-RuO_x bifunctional mechanisms remain intact on Au@PtRuNi. In contrast, the emergence and growth of the ~566 cm^{-1} band on Au@PtRuNi, but not on Au@PtRu, points to an additional, possibly more "upstream" role of Ni (oxy)hydroxides. The potential ranges for $Ni(OH)_2$ and NiOOH formation in literature strongly suggests that Ni in Au@PtRuNi is transformed in situ into $Ni(OH)_2$ [38,41,44].

Under this hypothesis, active surface of Au@PtRuNi can be viewed as a Pt-RuO_x-$Ni(OH)_2$ ensemble. In our electrochemical experiments, HOR has higher reaction activity on Au@PtRuNi than on Au@PtRu; our DFT results (Note #2 and Supplementary Figure S2 in supplementary materials) also show that the Pt-RuO_x-$Ni(OH)_2$ ensemble has modestly more favorable Gibbs free energies for OH adsorption and for $H_{ad} + OH_{ad} \rightarrow H_2O$ formation at the $Ni(OH)_2$/RuO_x interface, compared to RuO_x surface alone. In addition, we performed RT-TDDFTB simulations of four core-shell nanoparticle models: Au_{561}, $Au_{309}@Pt_{252}$, $Au_{309}@Pt_{216}Ru_{36}$, and $Au_{309}@Pt_{116}Ni_{116}Ru_{20}$ (Note #3 and Supplementary Figure S3 in supplementary materials). The results show that alloying the Au surface with Pt, Ru, and Ni does not produce a distinct new visible resonance, but instead broadens and damps the optical response of the Au core. This suggests that the enhanced HOR activity and the appearance of the 566 cm^{-1} Raman band are unlikely to originate from a stronger plasmonic or optical antenna effect. The optimized multi-metal clusters also exhibit significant structural relaxation upon incorporation of Ru and Ni, which may support the formation and stabilization of catalytically relevant species.

The role of $Ni(OH)_2$ can be rationalized by the Pt/$Ni(OH)_2$ system studied by Markovic's group both in HOR and hydrogen evolution reaction (HER) electrocatalysis [27,47]. Tian et al's research also reported synergistic interaction between RuO_x and $Ni(OH)_2$ in their system [48]. In both Markovic and Tian's systems, $Ni(OH)_2$ acts as a promoter that accelerates water activation and the production of OH_{ad} while Ru/RuO_x act as active sites for further reaction steps involving OH_{ad}. The spectroscopic evidence from the potential-dependent decrease in the 740 cm^{-1} OH_{ad} peak on Au@PtRuNi also validates our proposed multi-site bifunctional mechanism. Rather than simply increasing total OH_{ad} availability, $Ni(OH)_2$ actively regulates the supply-consumption network at the Pt-RuO_x sites. These results are consistent with DFT predictions of more favorable OH_{ad} reduction energetics at the $Ni(OH)_2$/RuO_x interface. To summarize, we successfully found spectroscopic evidence of Ni(II) forming in situ that correlates to increased HOR activity. Our in situ electrochemical SERS results, together with prior work on Pt/$Ni(OH)_2$ and Ru-NiO_x systems, support a multi-site bifunctional mechanism for HOR on Au@PtRuNi in which

View Article Online
DOI: 10.1039/D6NA00164E

$Ni(OH)_2$, RuO_x, and Pt play distinct yet complementary roles. In our Pt-RuO_x-$Ni(OH)_2$ framework formed in-situ from Au@PtRuNi catalyst, Pt provides sites for H adsorption, $Ni(OH)_2$ contributes to water activation and the supply of OH_{ad}, and RuO_x provides thermodynamically optimal adsorption sites for OH_{ad} to react with H_{ad} in the Volmer step. The $Ni(OH)_2$-Pt and $Ni(OH)_2$-RuO_x perimeters increase the number of interfacial H_{ad}/OH_{ad} pairs and establish a coupled OH_{ad} supply and consumption network. Taken together, our results support a multi-site, bifunctional mechanism and highlight a general strategy for future alkaline HOR catalyst design that not only promotes OH adsorption, but also focuses on the synergistic effect of different oxophilic components for coupled supply and consumption of OH_{ad}.

Acknowledgements

This research was supported by National Natural Science Foundation of China under Grant No. 22202167 and No. U24A20139, and National Key Research and Development Project of China under Grant No. 2023YFF0613603

References

1 J. Zhang, L. Shen, Y. Jiang and S.-G. Sun, *Nanoscale*, 2020, **12**, 19557–19581.

2 M. Z. Jacobson, W. Colella and D. M. Golden, *Science*, 2005, **308**, 1901–1905.

3 A. Soleimani, S. H. H. Dolatabadi, M. Heidari, A. Pinnarelli, B. M. Khorrami, Y. Luo, P. Vizza and G. Brusco, *Multiscale Multidiscip. Model. Exp. Des.*, 2024, **7**, 3153–3172.

4 M. İncı, *Sustain. Energy Technol. Assess.*, 2022, 53, 102739–102739.

5 Q. Liu, M. Ranocchiari and J. A. van Bokhoven, *Chem. Soc. Rev.*, 2021, 51, 188–236.

6 H. Prats and K. Chan, *Phys. Chem. Chem. Phys.*, 2021, 23, 27150–27158.

7 V. Hasannaeimi and S. Mukherjee, *Sci. Rep.*, DOI:10.1038/s41598-019-48582-7.

8 X. Mu, S. Liu, L. Chen and S. Mu, *Small Struct.*, DOI:10.1002/sstr.202200281.

9 C. A. Campos-Roldàn and N. Alonso-Vante, *Electrochem. Energy Rev.*, 2019, **2**, 312–331.

10 D. Weber, C. Dosche and M. Oezaslan, *J. Mater. Chem. A*, 2021, **9**, 15415–15431.

11 F. K. Bouho, T. Rafaïdeen, T. W. Napporn and C. Coutanceau, *Electrochimica Acta*, 2024, **498**, 144697–144697.

12 V. M. Truong, J. R. Tolchard, J. Svendby, M. Manikandan, H. A. Miller, S. Sunde, H. Yang, D. R. Dekel and A. O. Barnett, *Energies*, 2020, **13**, 582–582.

13 Y. Lian, *MATEC Web Conf.*, 2025, **410**, 1022–1022.

14 L. Osmieri, L. Pezzolato and S. Specchia, *Curr. Opin. Electrochem.*, 2018, **9**, 240–256.

View Article Online
DOI: 10.1039/D6NA00164E

15 J. Hyun and H.-T. Kim, *Energy Environ. Sci.*, 2023, **16**, 5633–5662.

16 L. Su, H. Wu, S. Zhang, C. Cui, S. Zhou and H. Pang, *Adv. Mater.*, DOI:10.1002/adma.202414628.

17 X. (Baohua) Zhang, X. Xiao, J. Chen, Y. Liu, H. Pan, W. Sun and M. Gao, *Energy Amp Environ. Sci.*, 2022, **15**, 4511–4526.

18 L. An, T. Zhao, W. Lei, C. Yang, J. Yang and D. Wang, *eScience*, 2025, **5**, 100400–100400.

19 Y. Fang, C. Wei, Z. Bian, X. Yin, B. Liu, Z. Liu, P. Chi, J. Xiao, W. Song, S. Niu, C. Tang, J. Liu, X. Ge, T. Xu and G. Wang, *Nat. Commun.*, DOI:10.1038/s41467-024-45873-0.

20 Z. Huang, S. Hu, M. Sun, Y. Xu, S. Liu, R. Ren, L. Zhuang, T.-S. Chan, Z. Hu, T. Ding, J. Zhou, L. Liu, M. Wang, Y. Huang, N. Tian, L. Bu, B. Huang and X. Huang, *Nat. Commun.*, DOI:10.1038/s41467-024-45369-x.

21 Y. Liao, S. Wang, Y. Zhang, Y. Zhang, Y. Gao, X. Mu, S. Liu, D. Wang and Z. Dai, *Adv. Sens. Energy Mater.*, 2023, **3**, 100089–100089.

22 W. J. F. Gannon and C. W. Dunnill, *Electrochimica Acta*, 2019, **322**, 134687–134687.

23 A. H. Shah, Z. Zhang, Z. Huang, S. Wang, G. Zhong, C. Wan, A. N. Alexandrova, Y. Huang and X. Duan, *Nat. Catal.*, 2022, **5**, 923–933.

24 J. Li, S. Ghoshal, M. K. Bates, T. Miller, V. Davies, E. Stavitski, K. Attenkofer, S. Mukerjee, Z.-F. Ma and Q. Jia, *Angew. Chem. Int. Ed.*, 2017, **56**, 15594–15598.

25 Y. Qiu, X. Xie, W. Li and Y. Shao, *Chin. J. Catal. Chin. VERSION*, 2021, **42**, 2094–2104.

26 W. Li, J. T. Feaster, S. A. Akhade, J. T. Davis, A. A. Wong, V. A. Beck, J. B. Varley, S. A. Hawks, M. Stadermann, C. Hahn, R. D. Aines, E. B. Duoss and S. E. Baker, *ACS Sustain. Chem. Eng.*, 2021, **9**, 14678–14689.

27 D. Strmčnik, M. Uchimura, C. Wang, R. Subbaraman, N. Danilovic, D. V. Vliet, A. P. Paulikas, V. R. Stamenković and N. M. Marković, *Nat. Chem.*, 2013, **5**, 300–306.

28 L. Shen, B.-A. Lu, X. Qu, J. Ye, J. Zhang, S. Yin, Q.-H. Wu, R. Wang, S.-Y. Shen, T. Sheng, Y. Jiang and S.-G. Sun, *Nano Energy*, 2019, **62**, 601–609.

29 Y. Feng, S. Lu, L. Fu, F. Yang and L. Feng, *Chem. Sci.*, 2023, **15**, 2123–2132.

30 X. Chen, X. Wang, J.-B. Le, S. Li, X. Wang, Y. Zhang, P. M. Radjenovic, Y. Zhao, Y. Wang, X.-M. Lin, J.-C. Dong and J. Li, *Nat. Commun.*, DOI:10.1038/s41467-023-41030-1.

31 L. Negahdar, C. M. A. Parlett, M. A. Isaacs, A. M. Beale, K. Wilson and A. F. Lee, *Catal. Sci. Technol.*, 2020, **10**, 5362–5385.

32 R. Wang, D. Li, S. Maurya, Y. S. Kim, Y. A. Wu, Y. Liu, D. Strmčnik, N. M. Marković and V. R. Stamenković, *Nanoscale Horiz.*, 2019, **5**, 316–324.

33 X.-M. Lin, X. Wang, Y.-L. Deng, X. Chen, H.-N. Chen, P. M. Radjenovic, X.-G. Zhang, Y. Wang, J.-C. Dong, Z.-Q. Tian and J. Li, *Nano Lett.*, 2022, **22**, 5544–5552.

34 Y. Wang, X.-T. Wang, H. Ze, X.-G. Zhang, P. M. Radjenovic, Y.-J. Zhang, J.-C. Dong, Z.-Q. Tian and J. Li, *Angew. Chem. Int. Ed.*, 2020, **60**, 5708–5711.

35 H. Zhang, S. Duan, P. M. Radjenovic, Z.-Q. Tian and J.-F. Li, *Acc. Chem. Res.*, 2020, **53**, 729–739.

36 M. Brust, J. Fink, D. Bethell, D. J. Schiffrin and C. J. Kiely, *J. Chem. Soc. Chem. Commun.*, 1995, 1655–1655.

37 G. Frens, *Nat. Phys. Sci.*, 1973, **241**, 20–22.

38 A. G. Oshchepkov, G. Braesch, A. Bonnefont, E. R. Savinova and M. Chatenet, *ACS Catal.*, 2020, **10**, 7043–7068.

39 D. S. Hall, D. J. Lockwood, C. Bock and B. R. MacDougall, *Proc. R. Soc. Math. Phys. Eng. Sci.*, 2015, **471**, 20140792.

40 D. S. Hall, C. Bock and B. R. MacDougall, *J. Electrochem. Soc.*, 2013, **160**, F235.

View Article Online
DOI: 10.1039/D6NA00164E

41 M. Alsabet, M. Grdeń and G. Jerkiewicz, *Electrocatalysis*, 2015, **6**, 60–71.

42 B. S. Yeo and A. T. Bell, *J. Phys. Chem. C*, 2012, **116**, 8394–8400.

43 D. S. Hall, D. J. Lockwood, S. Poirier, C. Bock and B. R. MacDougall, *J. Phys. Chem. A*, 2012, **116**, 6771–6784.

44 Y. Xue, L. Shi, X. Liu, J. Fang, X. Wang, B. P. Setzler, W. Zhu, Y. Yan and Z. Zhuang, *Nat. Commun.*, 2020, **11**, 5651.

45 Y. Men, Y. Tan, P. Li, Y. Jiang, L. Li, X. Su, X. Men, X. Sun, S. Chen and W. Luo, *Angew. Chem. Int. Ed.*, 2024, **63**, e202411341.

46 C. Yang, Y. Li, C. Ge, W. Jiang, G. Cheng, L. Zhuang and W. Luo, *Chin. J. Chem.*, 2022, **40**, 2495–2501.

47 N. Danilovic, R. Subbaraman, D. Strmcnik, K. Chang, A. P. Paulikas, V. R. Stamenkovic and N. M. Markovic, *Angew. Chem. Int. Ed.*, 2012, **51**, 12495–12498.

48 J. Tian, M. Wang, J. Xie, J. Hu, Z. Lu and Y. Cao, *Fuel*, 2025, **394**, 135019.

View Article Online
DOI: 10.1039/D6NA00164E

Figures:

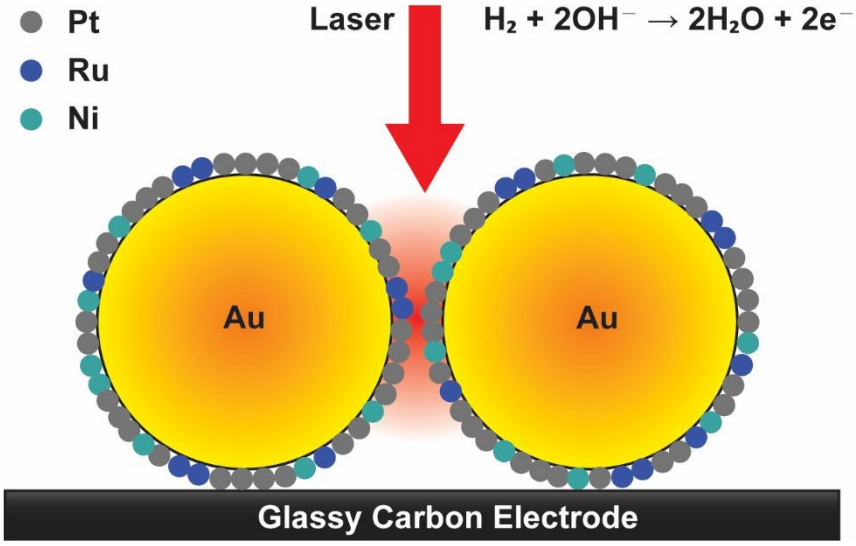

Figure 1. Illustrative schematic of HOR process on Au@PtRuNi surface in Alkaline media. (The choice for the size of Au core and Pt, Ru and Ni composition is related to the composition measured with EDS).

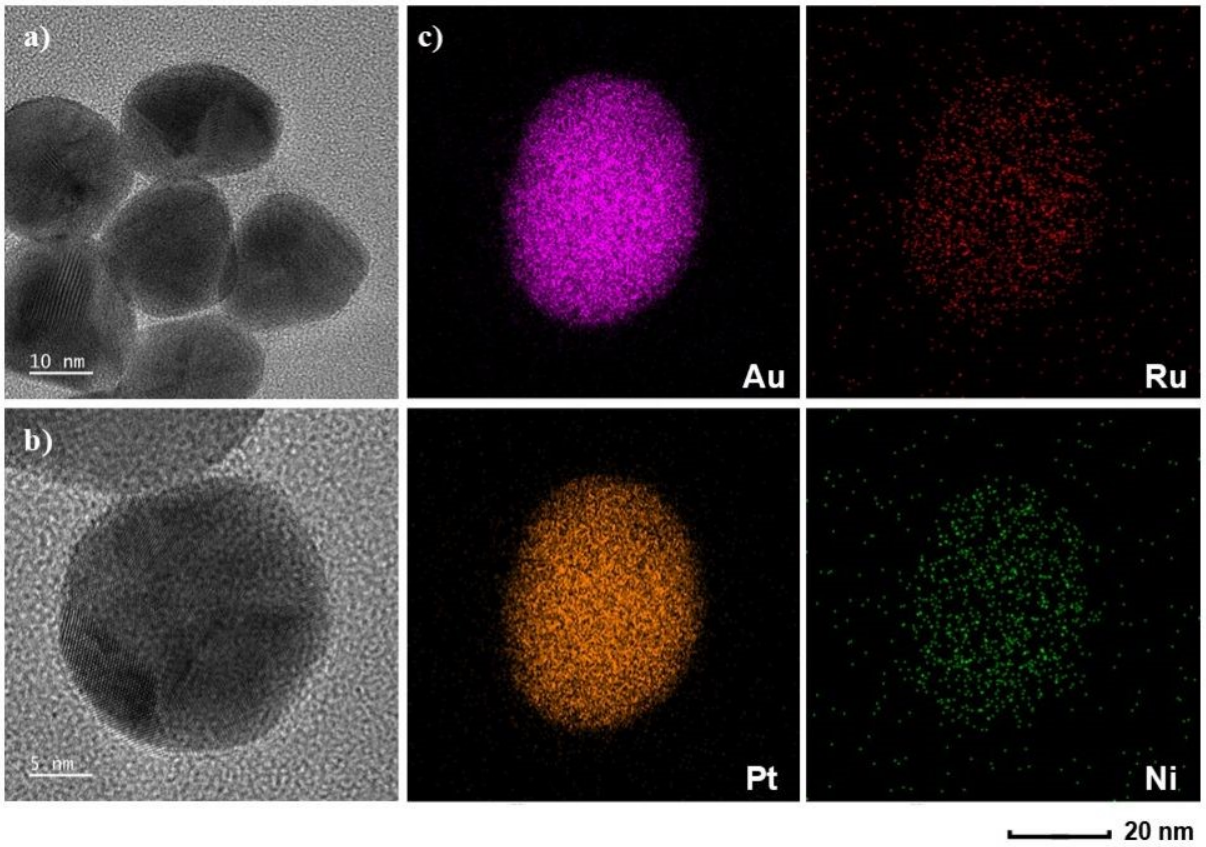

Figure 2 characterization of Au@PtRuNi nanoparticles. a) the TEM results of nanoparticles; scale bar: 10nm; b) the TEM results of one nanoparticle; scale bar: 5nm; c) elemental mapping from one single nanoparticle for Au, Pt, Ru and Ni, respectively; scale bar: 20nm.

View Article Online
DOI: 10.1039/D6NA00164E

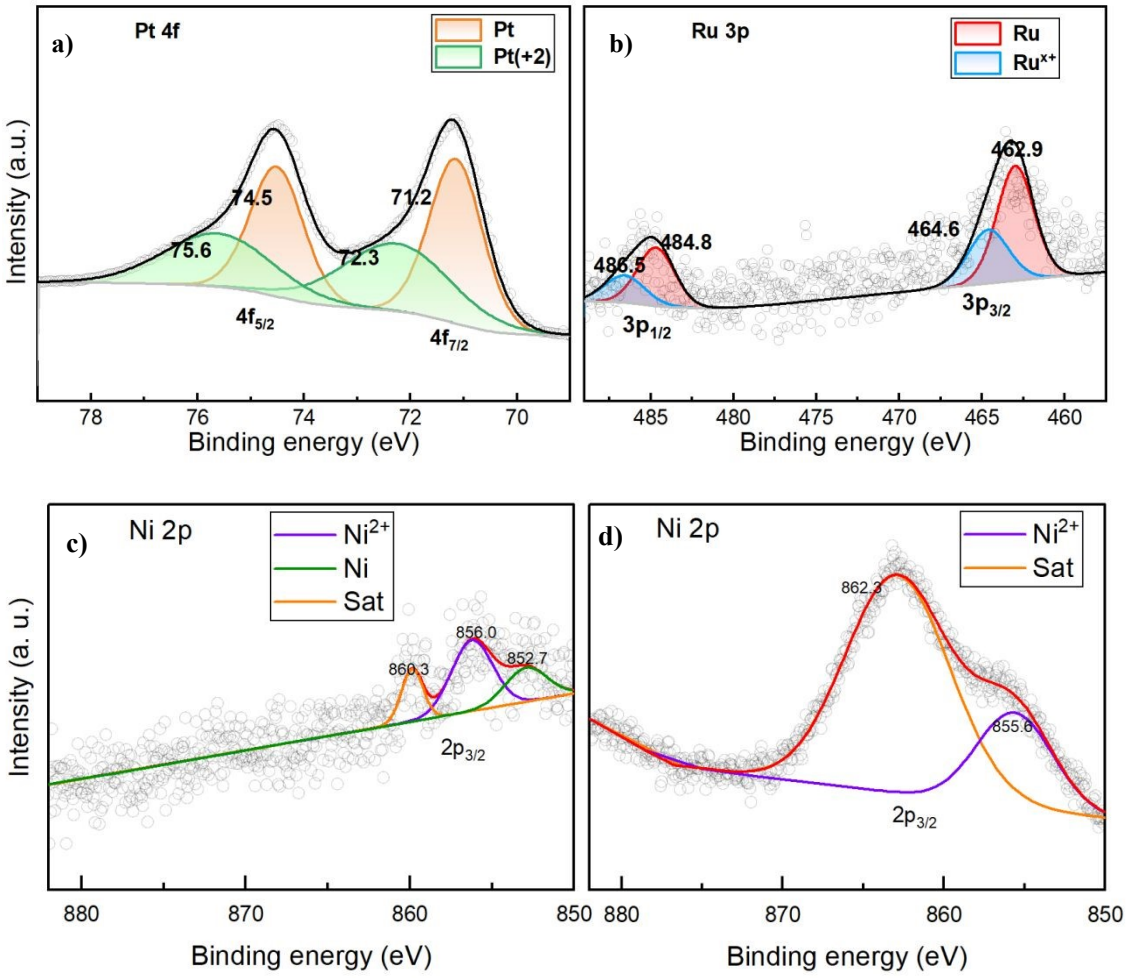

Figure 3 a) and b) XPS results of Pt 4f and Ru 3p of Au@PtRuNi nanoparticles, respectively; c) XPS result of Ni 2p of Au@PtRuNi nanoparticles, before HOR; d) XPS result of Ni 2p of Au@PtRuNi nanoparticles, after HOR;

View Article Online
DOI: 10.1039/D6NA00164E

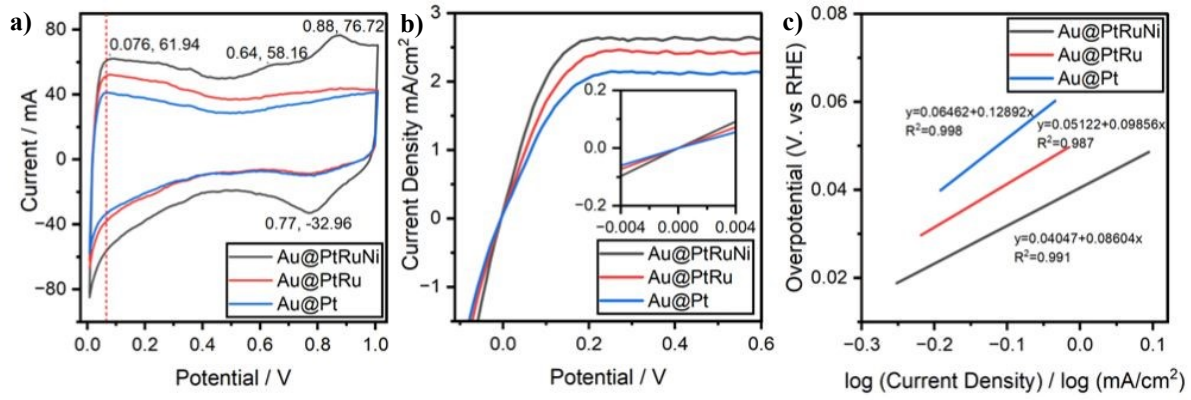

Figure 4 (a) cyclic voltammetry curves of Au@Pt, Au@PtRu and Au@PtRuNi, measured in a potential range from 0.05 to 1.0 V vs. RHE at a scan rate of 10 mV/s in 0.1 M KOH solution saturated with H_2; (b) Polarization curve obtained from linear sweeping voltammetry from -0.1 to 0.6 V vs. RHE at a scan rate of 10 mV/s and 1600 rpm rotation speed, inset is the micro-polarization region from -4 to 4mV; (c) Tafel plots derived from the HOR polarization curves normalized kinetic current densities.

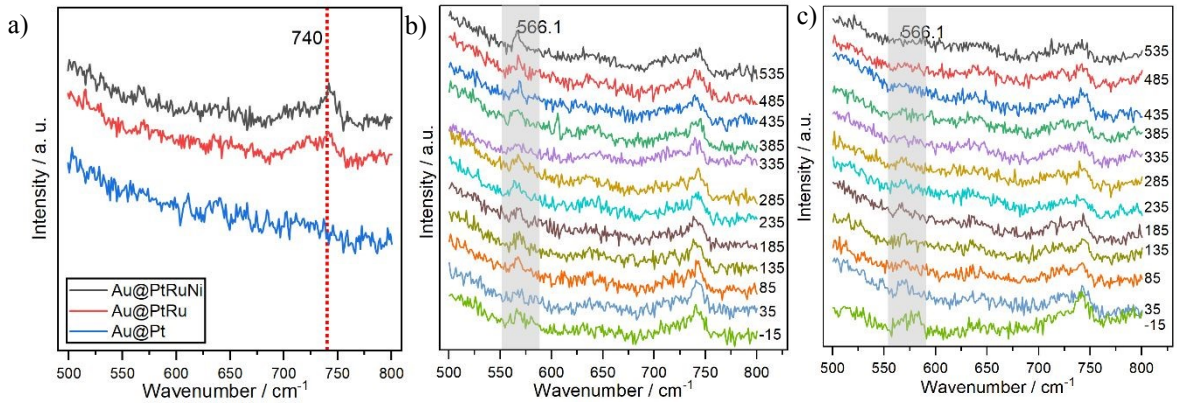

Figure 5 (a) Comparison between SERS spectra of HOR in Alkaline on different catalysts at 185 mV vs RHE potential; (b) and (c) the trend of SERS spectra of HOR in Alkaline on Au@PtRuNi and Au@PtRu catalyst, respectively, at different potentials from -15 to 535 mV vs RHE, with potentials(mV) at which the Raman spectra are taken are labeled to the right of each spectra.

View Article Online
DOI: 10.1039/D6NA00164E

Data Availability Statement

Data for this article are available on request.